Mechanical Properties of Nanostructured Metals: Molecular Dynamics Studies

18

Haofei Zhou and Shaoxing Qu

Contents

Abstract

This chapter overviews our recent work on MD simulations of the mechanical properties of nanostructured metals with an emphasis on revealing the controlling deformation mechanisms, interpreting the experimental data, and guiding further research in structural optimization and processing.

H. Zhou
School of Engineering, Brown University, Providence, RI, USA
e-mail: haofei_zhou@brown.edu

S. Qu (✉)
Department of Engineering Mechanics, Zhejiang University, Hangzhou, China
e-mail: squ@zju.edu.cn

C.-H. Hsueh et al. (eds.), *Handbook of Mechanics of Materials*,
https://doi.org/10.1007/978-981-10-6884-3_19

To achieve stronger and tougher metals by architecting their microstructures into the nanometer scale has been an enduring pursuit in materials science and engineering. During the past few decades, nanostructured metals have emerged as a new class of materials with tunable distribution of microstructures. Due to their unique microstructures, nanostructured metals could be prepared to exhibit an unusual combination of mechanical properties, such as ultrahigh strength, good tensile ductility, enhanced strain hardening, superior fracture toughness, and fatigue resistance [1–4]. However, the current lack of understanding of the underlying mechanisms that control the mechanical properties of these materials severely limits our ability to tailor or optimize their properties for specific applications.

Recent advances in computational modeling provide unprecedented opportunities to advance the frontier of knowledge in our understanding of mechanical behaviors of materials at nanoscales. With the development of teraflop computing power and sophisticated empirical atomic interaction potentials, large-scale molecular dynamics (MD) simulations have acted as an increasingly important role in complementing theories and experiments in tackling complex problems in computational materials science [5–8]. In this chapter, we will overview our recent work on MD simulations of the mechanical properties of nanostructured metals with an emphasis on revealing the controlling deformation mechanisms, interpreting the experimental data, and guiding further research in structural optimization and processing.

This chapter is organized as follows: Sections 1, 2, and 3 will cover a range of mechanical behaviors of nanotwinned metals along with several unique deformation mechanisms governed by nanoscale twin boundaries (TBs). Sections 4 and 5 will focus on the improvement of mechanical behaviors of metallic glasses (MGs) by introducing structural inhomogeneity into the glass matrix.

1 Strengthening by Nanoscale TBs

Nanoscale TBs are planar defects where atom arrangements on one side are mirror reflections of those on the other side. Ultrahigh strength and hardness have been reported in nanotwinned metals, ceramics, diamond, and biomaterials [9–19]. In response to the external loading, nanoscale TBs are known to hinder the movement of lattice dislocations that accommodate plastic deformation, thereby strengthen the polycrystals similar to traditional grain boundaries (GBs) in polycrystalline metals. Recently, it has been reported that there exists a transition in deformation mechanism from the conventional Hall-Petch strengthening mechanism to a dislocation-nucleation-governed softening mechanism that involves the nucleation and motion of twinning partial dislocations along the twin planes below a critical twin thickness [20, 21]. This transition in deformation mechanism has been demonstrated by experiments and simulations in nanotwinned polycrystalline metals with equiaxed grains where TBs and GBs are randomly oriented, as well as nanotwinned nanopillars and nanowires with only TBs but no other general GBs [22].

More recently, nanotwinned metals with columnar grains have been fabricated by direct current electrodeposition [23–25]. Such samples have a strong {111} out-of-plane texture and preferentially oriented nanoscale twins with TBs nearly perpendicular to the axial directions of the columnar grains. Columnar-grained nanotwinned Cu exhibits a remarkable plastic anisotropy and excellent fatigue properties, as their deformation behaviors are strongly dependent on the TB spacing and orientation. These phenomena provide a promising foundation to optimize the mechanical properties of nanotwinned materials by tailoring their twin microstructures. In the columnar-grained nanotwinned metals, when the loading direction is oriented in parallel to the twin planes, both dislocation pile-ups due to TB impediment and easy glide of partial dislocations along the twin planes are to a large extent suppressed, leading to the activation and glide of threading dislocations confined between neighboring TBs. A similar mechanism has been previously reported in nanolayered metallic composites where the plastic deformation is strongly associated with the glide of threading dislocation loops confined in the nanolayers [26, 27]. In these lamellar materials, the strength is enhanced as the layer thickness is reduced, which can be described by the so-called confined layer slip (CLS) model of threading dislocations [26].

This chapter will discuss the mechanical behavior of nanotwinned metals under uniaxial tension [28] and nanoindentation [29] loading conditions. It will be shown that the strengthening of nanotwinned metals is closely related to the deformation mechanisms governed by nanoscale TBs.

1.1 Threading Dislocation in Nanotwinned Metals

MD simulations were performed on fully three-dimensional (3D) Cu polycrystals. Each sample contains four columnar grains, where the coherent TBs are perpendicular to the axial direction of the grains (i.e., the thickness direction of the sample), exhibiting a strong {111} texture similar to the experiments [23–25]. The in-plane misorientations between neighboring grains are larger than 30° to ensure high-angle GBs. Uniaxial tension with a constant strain rate of $2 \times 10^8\ s^{-1}$ was applied parallel to the twin planes. Figure 1a, b shows dislocation structures in two representative grains in the sample with grain size $d = 50$ nm and $\lambda = 5.01$ nm at 6.18% strain. Most of the dislocation lines in Fig. 1a, b exhibit a hairpin-like shape. This kind of dislocation loops is generally referred to as threading or channeling dislocations. Figure 1c shows the atomic configuration of dislocation loops confined in twin lamellae. A typical threading dislocation has two misfit segments on the neighboring twin planes and one threading segment spanning across the twin lamella. During the simulation, threading dislocation loops are found to initiate from GBs, glide through grain interior, and become finally absorbed at the opposite GBs. Such deformation mechanism prevails in the samples with TB spacing larger than 3.75 nm.

In thin films [30, 31] or nanolayered metallic composites [23–25], the nucleation and motion of threading dislocation are known to be controlling mechanisms responsible for plastic deformation, resulting in enhanced strength with decreasing

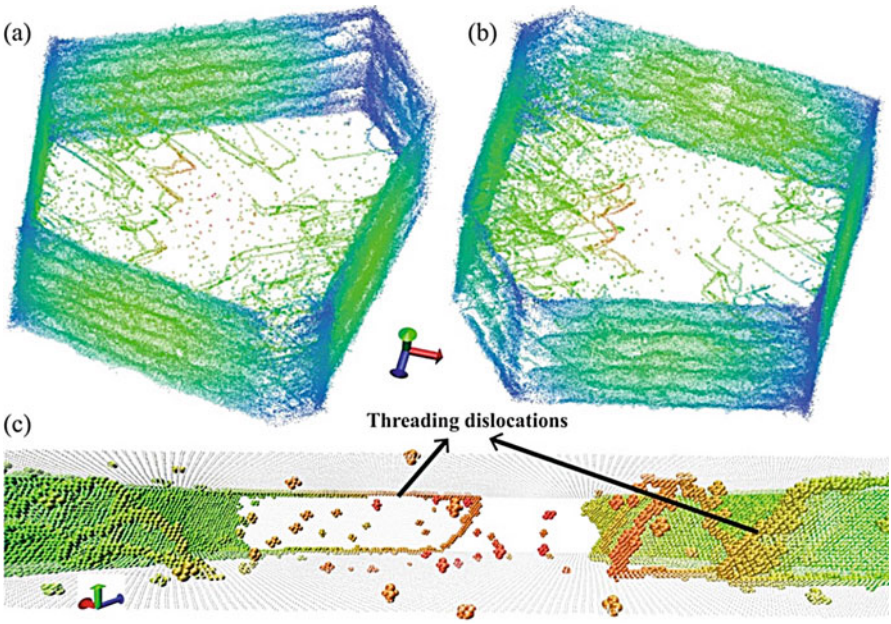

Fig. 1 (**a**, **b**) Dislocation structures in two representative grains of a simulated nanotwinned sample with $d = 50$ nm and $\lambda = 5.01$ nm at 6.18% train. (**c**) Atomic structures of threading dislocations in one twin lamella via position-based coloring, where the colors represent the distance of atoms from the center of a simulated grain. It is observed that two misfit segments lie on the twin planes and the threading segment is confined in the twin lamellae [28]

lamellar thickness. In the CLS model suitable for describing such size strengthening effect in thin films, the yield strength is expressed as [30, 31]

$$\sigma_{\mathrm{cls}} = M\left[\frac{\mu b \sin\varphi}{8\pi\lambda}\left(\frac{4-\nu}{1-\nu}\right)\ln\left(\frac{\alpha\lambda}{b\sin\varphi}\right) + \tau_0\right] \tag{1}$$

where λ is the film thickness, μ the shear modulus, ν the Poisson's ratio, τ_0 the resistance to dislocation glide from lattice and other obstacles, M the Taylor factor, φ the angle between slip plane and the layer interface, b the Burgers vector of dislocation, and α a coefficient representing the extent of dislocation core. For a nanolayered metallic composite, the CLS model is modified as [23–25]

$$\sigma'_{\mathrm{cls}} = M\frac{\mu b \sin\varphi}{8\pi\lambda}\left(\frac{4-\nu}{1-\nu}\right)\ln\left(\frac{\alpha\lambda}{b\sin\varphi}\right) - \frac{\gamma}{\lambda} + \frac{\mu b}{l(1-\nu)} \tag{2}$$

after the influence of interfaces is accounted for. The first term on the right-hand side of Eq. 2, similar to that of Eq. 1, represents the stress required to drag the misfit segments of a threading dislocation. The second term represents the prestress associated with the interfaces, with γ being the interfacial energy (J/m^2). The third

term reflects the interaction between a glide threading dislocation and a pre-existing array of misfit dislocations on the interfaces, with l denoting the mean dislocation spacing. For a twin lamellae with thickness on the order of several nanometers, the interfacial energy of TB being $\gamma_T = 24.0$ mJ/m^2 for Cu [32], the contribution from the second term in Eq. 2 to strength is negligible. Therefore, regarding the last two terms in Eq. 2 as a constant σ_d independent of TB spacing, one may rewrite Eq. 2 as [28]

$$\sigma_{cls}^{TB} = M\frac{\mu b \sin\varphi}{8\pi\lambda}\left(\frac{4-\nu}{1-\nu}\right)\ln\left(\frac{\alpha\lambda}{b\sin\varphi}\right) + \sigma_d \tag{3}$$

In subsequent analysis, we will use Eq. 3 to account for the strengthening due to threading dislocations confined in twin lamellae.

1.2 Jogged Dislocation in Nanotwinned Metals

Figure 2 shows deformation patterns in two representative grains in the sample with $d = 50$ nm and $\lambda = 0.83$ nm at 10.30% strain, which is very distinct from those shown in Fig. 1. It is observed that the plastic deformation is governed by activities of necklace-like dislocations extending over multiple twin planes, which we refer to as jogged dislocations. Each of these jogged dislocations is nucleated as a whole from a GB, rather than through assembly or interactions of separately emitted dislocations. The nucleation process should be assisted by diffusion and coalescence of vacancies.

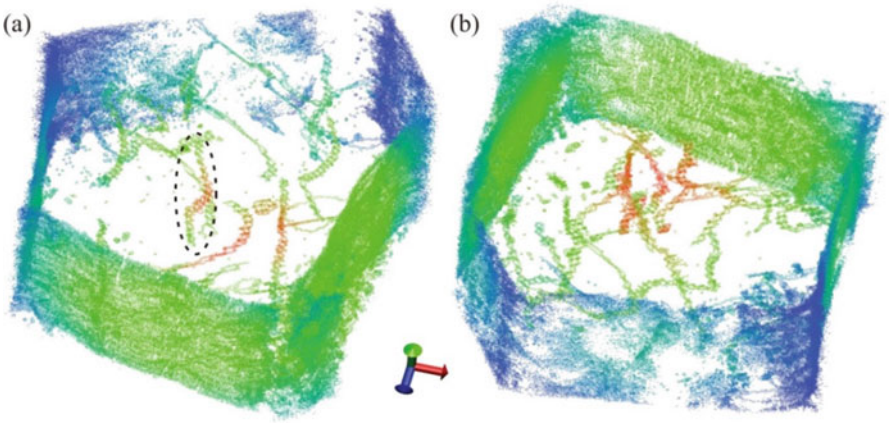

Fig. 2 (**a**, **b**) Dislocation structures in two representative grains of a simulated nanotwinned sample with $d = 50$ nm and $\lambda = 0.83$ nm at 10.30% strain. Multiple extended dislocations connect with each other, constituting a jogged dislocation. Atoms are painted via the position-based coloring method [28]

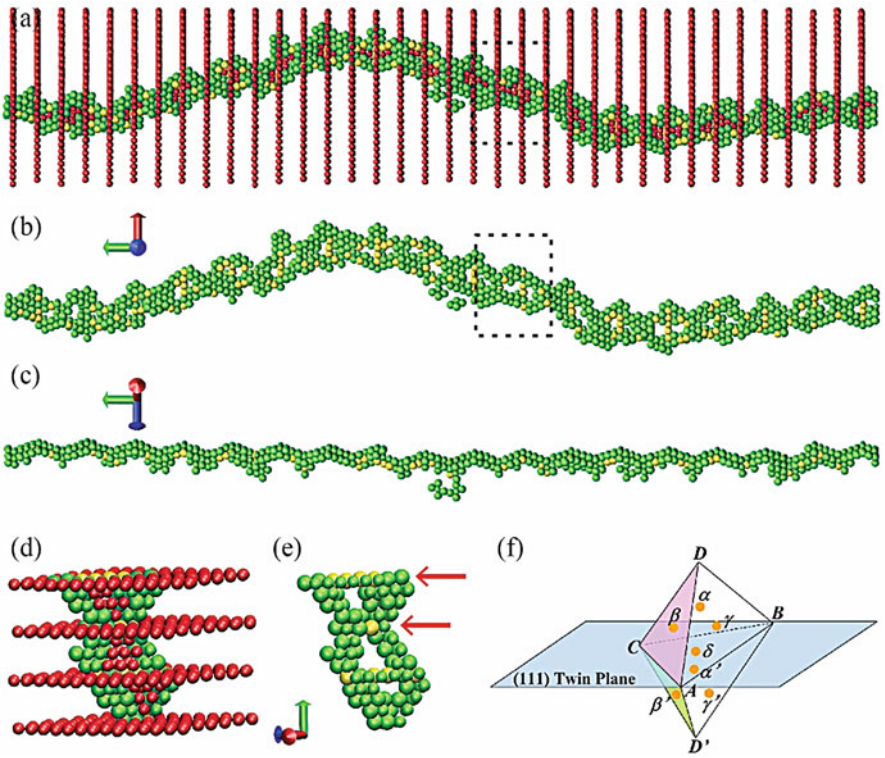

Fig. 3 (**a**–**c**) Detailed atomic structures of a jogged dislocation (circled in Fig. 2a) from different views. The jogged dislocation exhibits a zigzag shape from a certain perspective. (**d**–**e**) Magnification of the segments within the dashed line frames in (**a**) and (**b**). The extended and constricted jogs of one segment are indicated by the red arrows. (**f**) Double Thompson tetrahedron representation in the twin-matrix system. The upper tetrahedron represents the slip systems for the matrix, while the lower one for the twin. Colors are assigned to atoms based on their local crystal orders measured by the common neighbor analysis (CNA) method: gray stands for perfect atoms, red for atoms in stacking faults or TBs, green for atoms in dislocations or GBs, blue for atoms near vacancies, and yellow for fully disordered atoms [28]

Figure 3a, b shows the detailed atomic structures of a single-jogged dislocation spanning across multiple twin planes, while Fig. 3c, d shows the magnification of three consecutive segments of the jogged dislocation. The dislocation pattern consists of multiple extended dislocations, each bounded by two twin planes. Every extended dislocation contains a pair of leading and trailing partial dislocations separated by a stacking fault. Because of the geometrical constraints, each extended dislocation is terminated at a twin plane and joined with another dislocation in the neighboring twin through a common segment in the twin plane. Based on the double Thompson tetrahedron representation in Fig. 3e, the leading and trailing partials in matrix have Burgers vectors of $A\beta$ and βC, while those in the twin plane have Burgers vectors of $A\beta'$ and $\beta' C$. Thus, the common segment in the twin plane has

the Burgers vector of a stair-rod dislocation $\boldsymbol{\beta}'\boldsymbol{\beta}$. Such stair-rod segment possesses the characteristic of a unit jog and is pinned at the twin plane. Depending on its Burgers vector and the corresponding line tension, the unit jog may be either of extended or constricted type, as illustrated in Fig. 3d. Plastic deformation governed by jogged dislocations prevails for TB spacings below 3.75 nm. Interestingly, the motion of jogged dislocation involves the collective movements of multiple extended dislocations which are linked by numerous unit jogs pinned at twin planes. As the extended part of a jogged dislocation is driven forward by the applied stress, the unit jogs undergo de-pinning at the twin planes, which is assisted by diffusion of point defects.

1.3 Twin-Size Induced Transition in Dislocation Mechanism and Continuous Strengthening in Nanotwinned Metals

Comparison between Figs. 1 and 2 demonstrates that there exists a distinct transition from threading dislocation to jogged dislocation governed deformation mechanisms as the twin thickness is reduced. Figure 4a shows typical stress-strain curves of the samples with $d = 20$ and 30 nm. If we take the average of stresses after yielding as the flow stress, it is observed from Fig. 4b that the flow stress gradually increases with deceasing TB spacing. This means that the presence of TBs always strengthens the columnar-grained nanotwinned metals if the external loading is parallel to the TBs, in contrast to the softening phenomenon previously revealed in the equiaxed nanotwinned metals in the similar range of twin thickness [20, 21]. We find that the CLS model in Eq. 3 fails to correlate the size dependence of materials strength in Fig. 4b. In fact, the prediction from Eq. 3 is found to decrease when TB spacing λ falls below a certain value, as shown in Fig. 4b. As the layer thickness becomes comparable to the cutoff radius of dislocation core, the first term in Eqs. 1 and 3 becomes negative due to the logarithmic component, causing a stress drop which is

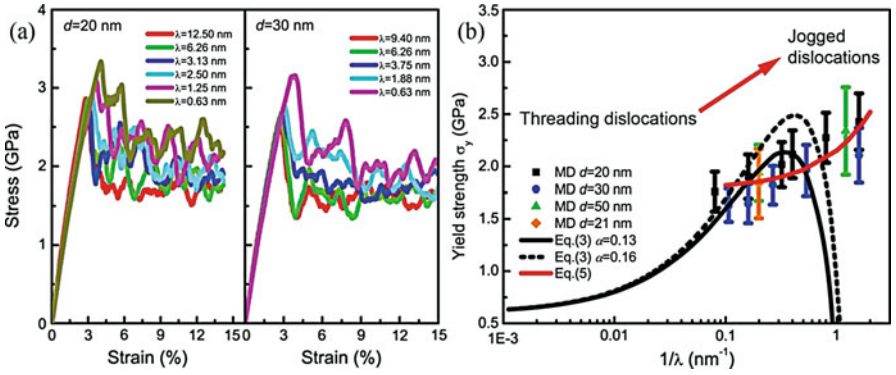

Fig. 4 (**a**) Stress-strain curves of simulated samples with $d = 20$ and 30 nm and a range of TB spacings from 0.63 nm to 12.50 nm. (**b**) The twin-size dependence of material strength. There exists a transition from threading dislocation to jogged dislocation governed deformation regimes with reduced TB spacing [28]

Table 1 Parameters used in Eqs. (3) and (5) for Cu [28]

μ (GPa)	ν	b (nm)	φ	α
48	0.35	0.147	70.5°	0.13, 0.16
M	σ_d (GPa)	τ_0 (GPa)	b_f (nm)	f_{pin} (pN)
3	0.60	0.59	0.255	31.48

contradictory to our simulation results. Relevant parameters used in Eq. 3 are summarized in Table 1.

The deformation patterns shown in Fig. 2 imply that the strengthening of a columnar-grained nanotwinned metal, as the TB spacing is reduced to around 1 nm (comparable to the cutoff radius of dislocation core), must be associated with the collective motion of jogged dislocations. Consequently, the CLS model is no longer valid at sufficiently small TB spacings (see Fig. 4b) due to a transition in deformation mechanism. To explain the above TB strengthening behavior, especially in the small twin-thickness range, we propose a simple model based on the motion of jogged dislocation and de-pinning of unit jogs on twin planes. For every constituent loop in the jogged dislocation, the pinning force f_{pin} exerted by TBs on the unit jog during its motion is compensated by the associated Peach-Koehler force acting on the dislocation. Accordingly, the equilibrium equation of a dislocation should be given by [28]

$$f_{pin} = (\tau - \tau_0) b_f \lambda \tag{4}$$

where τ is the resolved shear stress, τ_0 the friction stress, and b_f the magnitude of Burgers vector of dislocation. Here the subscript "f" in b is used to emphasize the full-dislocation nature of the jogged dislocation. Solving Eq. 4 and considering the Taylor factor M, we obtain the following steady-state flow stress σ_{jog} due to the de-pinning process [28]

$$\sigma_{jog} = M\left(\frac{f_{pin}}{b_f \lambda} + \tau_0\right) \tag{5}$$

As shown in Fig. 4b, as the TB spacing falls below 3.75 nm, the strength enhancement can be well described by Eq. 5 with $f_{pin} = 31.48$ pN and $\tau_0 = 0.59$ GPa for the case of Cu. Based on our simulations and the theoretical predictions in Fig. 4b, the transition from threading to jogged dislocations occurs around 2–5 nm. Within this regime, the threading and jogged dislocations could coexist during plastic deformation. As the TB spacing is reduced across this size range, the dominant mechanism of plastic deformation gradually transits from a threading dislocation-dominated regime to one that is fully dominated by jogged dislocations throughout the grain interiors.

1.4 Nanotwinned Metals Under Nanoindentation

Strengthening effect governed by nanoscale TBs is also demonstrated in nanoindentation simulations on quasi-3D polycrystalline Cu samples with an idealized

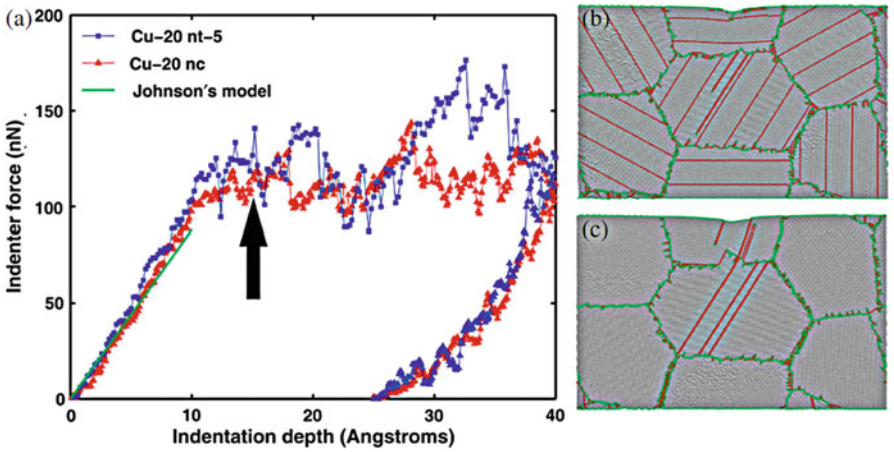

Fig. 5 (**a**) Simulated load-displacement curves of nanotwinned and twin-free samples under nanoindentation. (**b**–**c**) Deformation patterns of the samples at the moment indicated by the arrow in (**a**). Atoms are painted by the CNA method [29]

{110} texture. Each sample consists of 6 randomly oriented grains with a mean grain size of 20 nm, and the sample size is $60 \times 40 \times 2$ nm^3. During nanoindentation, a cylindrical indenter was pushed toward the top sample surface at a speed of 0.01 nm/ps until reaching a maximum indentation depth of 4 nm. Each Cu atom in the sample interacts with the rigid indenter via a repulsive potential $V(r) = A\theta(R\text{-}r)(R\text{-}r)^3$, where $A = 2.67$ nN/Å^2 is a constant, $\theta(R\text{-}r)$ is the standard step function, $R = 4$ nm is the indenter radius, and r is the distance between the atom to the center of the cylindrical indenter. The grain underneath the indenter is oriented such that its (111) planes are tangential to the indenter surface before contact. The vertical motion of ten layers of atoms at the bottom of the sample is fixed.

Figure 5a shows the load-displacement curves of two simulated samples. Sample "Cu-20 nt-5" has a TB spacing of 5 nm, while sample "Cu-20 nc" is twin-free. It is seen that the nanotwinned sample has a larger resistance to nanoindentation than the twin-free sample. Figures 5b, c show deformation patterns captured at the moment indicated by the arrow in Fig. 5a. It is seen that the dislocations in the nanotwinned grain in direct contact with the indenter are severely blocked by the nanoscale TBs (Fig. 5b). In the twin-free case, however, the dislocations can easily traverse the grain and interact with the GB on the other side of the grain (Fig. 5c).

2 Toughening by Nanoscale TBs

Experiments have reported that a high and controlled density of nanoscale TBs could serve to enhance the ductility and fracture toughness of nanocrystalline materials [33–35]. In this section, attention is focused on exploring the atomistic toughening mechanisms governed by nanoscale TBs in Ni nanocrystals by MD simulations [36].

2.1 Crack Propagation in Nanotwinned Metals

The fracture process of nanocrystalline Ni samples with and without nanoscale TBs is examined by MD simulations. Figure 6a shows a quasi-3D nanocrystalline Ni sample containing nanoscale TBs. The mean grain size is 20 nm, and the sample size is $80 \times 120 \times 1.99\ \text{nm}^3$. An initial edge crack with a length of 13 nm was introduced into the sample. At the beginning of each loading step, a displacement field acquired from the mode-I crack tip solution was applied to the boundary atoms within 1 nm from the edges of the sample. The increment in the stress intensity factor is $0.01\ \text{MPam}^{1/2}$. Afterward, the boundary atoms were fixed, while the other atoms were allowed to relax for 1 ps. It is observed that a high density of TBs with inclined TB orientations can greatly enhance the fracture toughness of polycrystalline Ni (Fig. 6b, c). The detailed atomistic toughening mechanisms governed by nanoscale TBs will be discussed in Sect. 2.2.

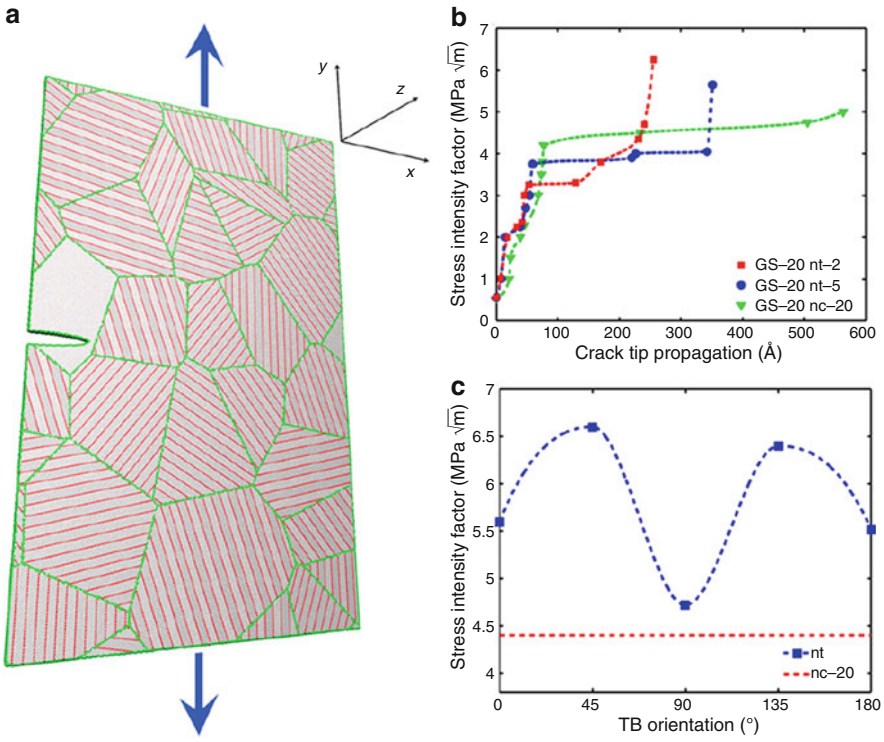

Fig. 6 (**a**) Quasi-3D nanotwinned Ni polycrystals with a TB spacing of 2 nm. The blue arrows indicate the direction of the externally applied stress. (**b**, **c**) Stress intensity factor versus crack tip propagation distance for samples with different TB densities and orientations [36]

2.2 Toughening Mechanisms Governed by Nanoscale TBs

Dislocation motion along TBs is found to be an effective way to release the stress concentration at the crack tip. Figure 7a shows that plastic deformation is largely suppressed in nanocrystalline Ni samples without nanoscale TBs. In nanotwinned Ni samples, however, numerous partial dislocations are emitted from the TB-GB intersections and glide along the nanoscale TBs, leading to crack blunting as shown in Fig. 7b.

The failure mechanism in nanocrystalline Ni samples switches from intergranular fracture to intragranular fracture as the TB density increases (Fig. 7). In twin-free nanocrystalline Ni sample, the crack propagates along the GBs (Fig. 7a), while in nanotwinned samples with high density of TBs, the crack tends to propagate along or through the nanoscale TBs within the grains (Fig. 7b). The GB energy of Ni predicted by the EAM potential is 1572 mJ/m^2, much higher than its TB energy of 63 mJ/m^2. The substantial difference between these boundary energies suggests that the crack extends along an intergranular path. However, a high density of TBs near the crack tip is able to promote local nucleation and motion of dislocations, hindering the intergranular fracture mechanism in nanotwinned Ni samples. The dislocation motion along the TBs, on the other hand, may disturb the coherency of the TBs and trigger intergranular fracture during crack blunting.

Another toughening mechanism revealed in nanotwinned Ni samples is the nucleation and growth of an incipient daughter crack in the grain ahead of the mother crack (Fig. 7b). The formation of the daughter crack is associated with a sequence of partial dislocations gliding along a TB, squeezing into a TB-GB intersection, and creating a local wedge-shaped crack embryo. As the daughter crack grows, the neighboring TBs become curved, and numerous partial dislocations

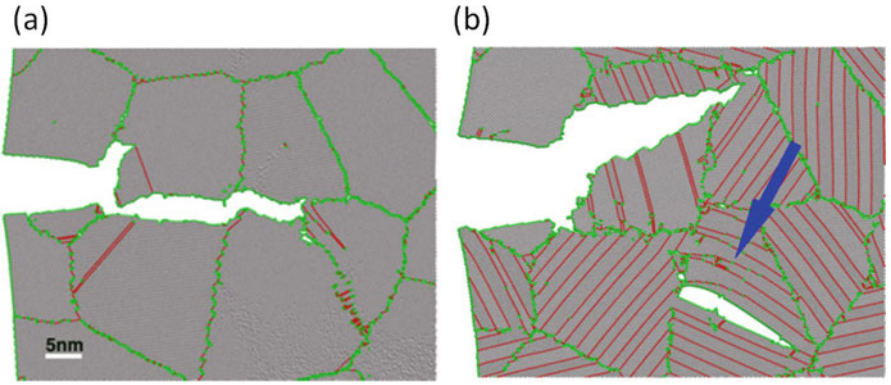

Fig. 7 (**a**) Twin-free nanocrystalline Ni showing limited plastic deformation. (**b**) Nanotwinned Ni exhibiting crack blunting and intragranular fracture with numerous dislocations gliding along TBs. TBs become curved (indicated by the arrow) due to the growth of a daughter crack ahead of the main crack [36]

are deposited along these TBs (indicated by the arrow in Fig. 7b), forming geometrically necessarily dislocations. This provides an effective toughening mechanism that locally accommodates a large amount of plastic deformation.

3 Delocalized Deformation in Nanotwinned Metals

Localized deformation is one of the most frequent causes of material failure in metallic components and structures. How to maintain sustained deformation in nanostructures without localized failure is an important question for many applications of nanotechnology. MD simulations demonstrated that nanoscale TBs in one-dimensional nanostructures can lead to giant rotational deformation without localized failure through a novel torsional detwinning domino mechanism [37].

3.1 Torsion of Nanotwinned Nanorods

Figure 8a shows the typical surface morphology of a twisted nanotwinned nanorod with diameter $D = 20$ nm. TBs are embedded in the nanorod with uniform spacing of $\lambda = 1.05$ nm and aligned nearly perpendicular to the axis of the cylindrical nanorod with a tilt angle less than $\pm 5°$. A constant surface shear strain rate of $3.33 \times 10^7\ s^{-1}$ was adopted to twist the nanorod to a total surface shear strain of 420%. It is seen that the surface becomes rough with numerous slip steps. The average depth of the slip

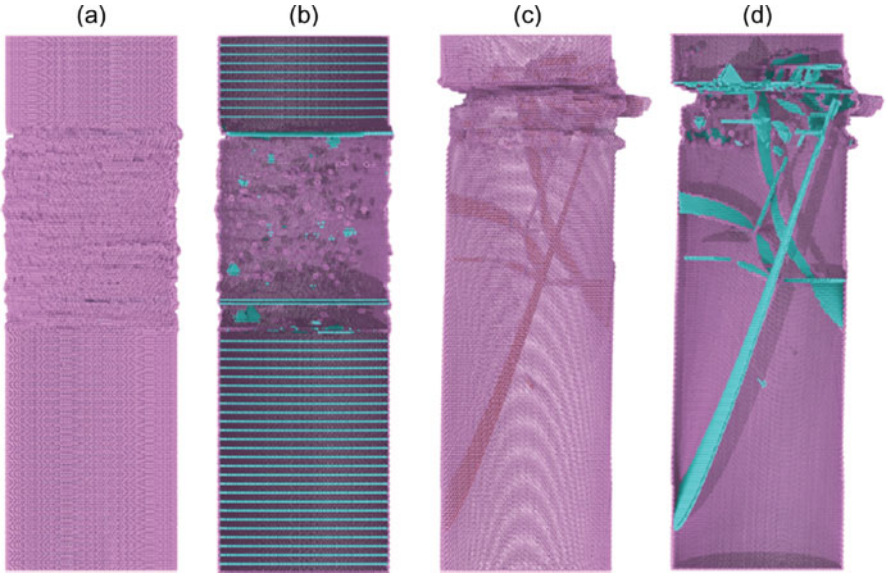

Fig. 8 Deformation patterns of nanotwinned (**a**, **b**) and single-crystalline (**c**, **d**) nanorods after being loaded by torsion to 420% of surface shear strain [37]

steps are on the order of 1 nm. The roughness is associated with the depletion of TBs (i.e., detwinning) during torsion, as indicated by Fig. 8b. It is clear that all twin planes underneath the rough surface have been dissolved, leaving an "infected" region filled with various types of lattice defects. Similar plastic deformation patterns were observed in all simulated nanotwinned nanorods. For comparison, the deformation patterns of a twisted single-crystalline twin-free counterpart were also displayed in Fig. 8c. The surface of the twin-free nanorod after torsion is featured by a few slip ledges, which have much larger scales (about 5 nm in depth) and are distributed much more narrowly than those observed in Fig. 8a. This implies that the plastic deformation is localized to several atomic planes in the twin-free samples. The "infected" region is filled with a few stacking fault ribbons and dislocation lines, as shown in Fig. 8d.

Figure 9a shows the surface shear stress versus strain relations of nanotwinned and single-crystalline nanorods during torsion. The shear stress and shear strain at the surface are given by $\tau = 2\,T/\pi R^3$ and $\varepsilon = \kappa R$, respectively, where T is the torque, κ is the twist per unit length, and R is the radius of the nanorod. It is observed from Fig. 9a that both samples responded cyclically to the external load with a period of about 17.5% strain, corresponding to a twist angle of 60°. In each cycle of the stress-strain curve of the twin-free samples, a number of dislocations nucleated from the surface and then reacted with each other, leading to dislocation multiplication and formation of complex dislocation networks on the (111) plane. In contrast to the twin-free samples, it is seen that each cycle on the stress-strain curve of the nanotwinned samples corresponds to the depletion of one TB, as evidenced by Fig. 8b. Figure 9b–g shows the shear strain contours on the axial sections of the twisted nanorods, where atoms are colored according to their local von Mises strain values. The twist-induced strain gradient along the radial direction is clearly identified. For the nanotwinned nanorod, detwinning started at a TB near the middle of the nanorod, which was transformed into a twist boundary to accommodate a certain amount of plastic strain. Further deformation caused the twisted boundary to disappear, and the original TB was dissolved. The same detwinning process then spread on after the other into the neighboring TBs under increasing torsion, as shown in Fig. 9b–d. Plastic deformation was accumulated and delocalized through the consecutive depletion of TBs in the "infected" region outlined by a dashed box in Fig. 9b. This is contrast to the highly localized plastic deformation in the single-crystalline nanorod, as shown in Fig. 9e–g. More interestingly, only one TB is depleted in the nanotwinned nanorod for every 60° of torsion, which may be referred to as a single detwinning event. Every detwinning event sets off a subsequent detwinning event on a neighboring TB, leading to a detwinning domino propagating along the nanorod.

Each peak in the stress-strain curves shown in Fig. 9a corresponds to dislocation nucleation on a TB. A significant difference between the two curves in Fig. 9a is that the peak stress remains at about 2.0 GPa throughout the torsion for the nanotwinned nanorod, while it decreases gradually from as high as 3.2 GPa in the first cycle to less than 1.3 GPa at the end for the single-crystalline nanorod. The reduction in the peak stresses of the twin-free sample implies that dislocations there can nucleate and multiply with ease due to progressive strain localization and accumulation of defects.

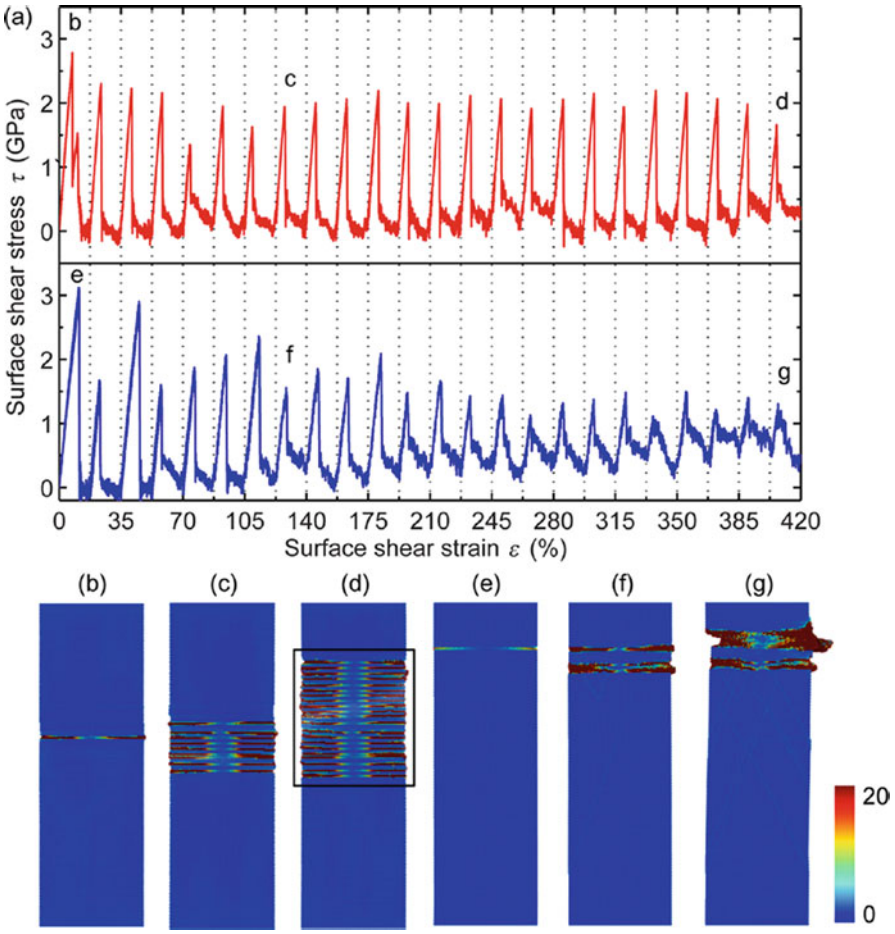

Fig. 9 (**a**) Stress-strain relations of nanotwinned (top) and single-crystalline (bottom) nanorods under torsion. (**b**–**d**) Atomic shear strain contours of nanotwinned nanorods during twisting. (**e**–**g**) Atomic shear strain contours of single-crystalline nanorods during twisting [37]

However, the peak stresses of the nanotwinned sample remain at a nearly constant stress level associated with the onset of individual detwinning event.

3.2 Physical Origin of the Torsional Detwinning Domino in Nanotwinned Nanorods

Figure 10 illustrates the physical nature of the twist-induced detwinning process in nanotwinned nanorod under torsion. First imagine a typical nanotwinned structure with a stacking sequence of CABCBAC. Figure 10a shows a diagram of three

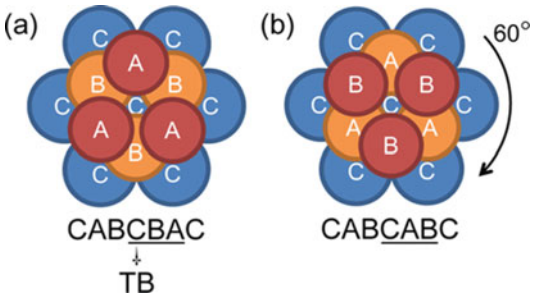

Fig. 10 Physical mechanism of twist-induced detwinning. (**a**) Three adjacent (111) atomic layers arranged in a twinned structure. (**b**) The same stack of atomic layers arranged in a perfect fcc structure after a twist of 60° in imposed on the layers above the twin plane C [37]

consecutive (111) layers. If all atomic layers above the twin plane C are rigidly twisted by an angle of 60°, the resulting configuration is shown in Fig. 10b. It is seen that the mirror symmetry across the twin plane C has been removed. The final stacking sequence is CABCABC, recovering the perfect fcc structure. Thus, the detwinning domino essentially originates from the rotational symmetry of {111} planes in fcc metals.

Figure 11 shows a series of snapshots that capture the structural evolutions of a TB at various strain levels. Initially, a partial dislocation nucleates from the free surface and glides along the TB, as shown in Fig. 11a. This dislocation is then trapped at the center due to the stress gradient in the radial direction. Meanwhile, another partial dislocation nucleates from the free surface, as shown in Fig. 11b. More partial dislocations emit from the free surface and react with each other, leading to the formation of dislocation junctions indicated in Fig. 11c. Each arm of the junction is an extended dislocation consisting of leading and trailing partial dislocations separated by a stacking fault. As more dislocations interact with the pre-existing dislocation structures, a complex dislocation network becomes visible in Fig. 11d. Crystallographically, such dislocation network corresponds to a high-angle twist boundary. The partial dislocations in the network are geometrically necessary to accommodate the lattice mismatch between the original TB and the adjacent (111) plane. A twist from 0° to 30° gradually dismantles the coherency of the TB, which results in a fully disordered configuration shown in Fig. 11e. Interestingly, when the twist angle increases from 30° to 60°, the dislocation network gradually coarsens as dislocations progressively escape from the free surface, as shown in Figs. 11f–h. Such phenomenon is accompanied by a significant drop in the applied shear stress after yielding (Fig. 9a). The final configuration after twisted by 60° is just a perfect fcc structure. It is noted that each detwinning event is mediated by the formation and annihilation of a twist boundary and intense dislocation interactions occur during the detwinning process, leading to the formation of various types of defects, such as vacancies, stacking fault tetrahedrons (SFTs), and even extrinsic stacking faults (ESFs), as shown in Fig. 11i.

To understand why detwinning occurs sequentially, rather than randomly at any twin planes, the distribution of shear stress $\sigma_{\theta z}$ in the twisted nanotwinned nanorod is plotted in Fig. 12. Significant stress concentration is found at the intersections between TBs and the free surface. More importantly, the maximum $\sigma_{\theta z} = 3.56$ GPa

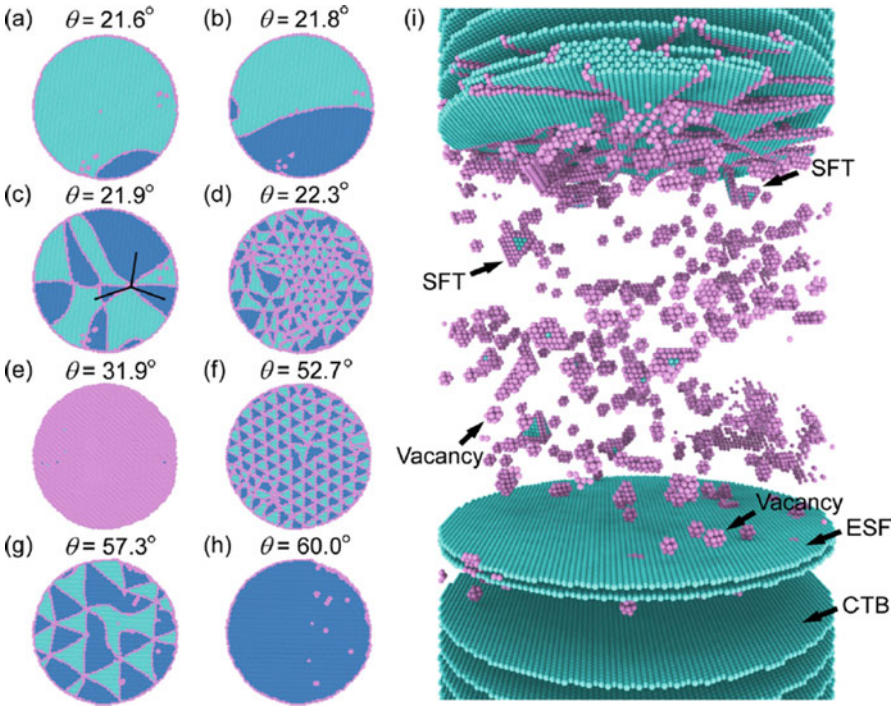

Fig. 11 Structural evolution of a twin plane in a twist-induced detwinning event. (**a**, **b**) Nucleation of partial dislocations from the free surface. (**c**, **d**) Formation of dislocation junctions due to dislocation interactions. (**e**) Atomic configuration of TB after twisting by ~30°. (**f**, **g**) Coarsening of dislocation network as dislocations escape from the surface. (**h**) Depletion of TB after twisting by 60°. (i) Abundant residual lattice defects in the "infected" region after a series of detwinning events [37]

occurs at the outermost TB of the nanotwinned region, about 0.5 GPa higher than that on the rest of the TBs. This induces detwinning always at the edge of the nanotwinned region, leading to the observed sequential detwinning.

The torsional detwinning domino in nanotwinned nanorods departs from all previously reported detwinning mechanisms [20, 38, 39] in that it does not require TB migration. Instead, detwinning is realized through sequential transformation (into a twist boundary) and annihilation of TBs with a rotational period of 60°, which contributes to the delay of shear localization in the nanostructure. The sequential depletion of TBs leads to a sustained rotational plastic deformation. Take a nanorod containing a total of 60 TBs and with diameter/length = 1/3, for instance; the complete depletion of these coherent interfaces via the domino detwinning mechanism gives rise to ~1000% of plastic strain. Thus, the operation of a detwinning domino could lead to practically unlimited rotational deformation in 1D nanostructures.

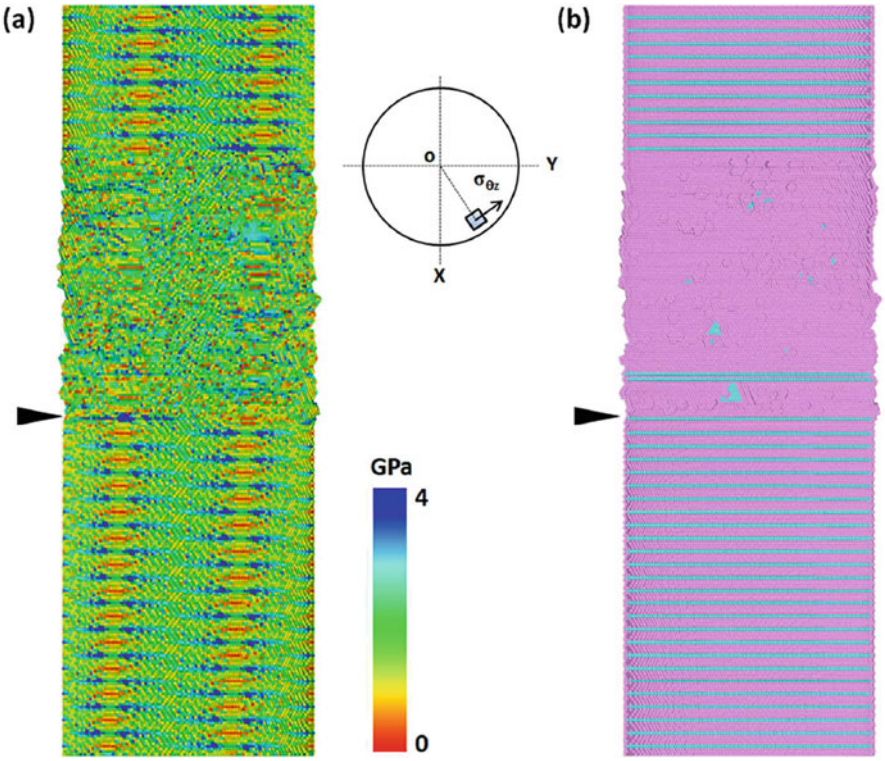

Fig. 12 Distribution of virial shear stress $\sigma_{\theta z}$ in a twisted nanotwinned nanorod right before the next detwinning event occurs at the twin plane indicated by the black arrows. (**a**) Color map of $\sigma_{\theta z}$ revealing stress concentration at the intersections between TBs and the free surface. The maximum $\sigma_{\theta z}$ occurs at the outermost TB of the nanotwinned region indicated by the black arrow. The topright schematic depicts the stress component $\sigma_{\theta z}$ that is calculated to draw the stress contour. (**b**) Sliced nanotwinned nanorod exposing the intersections between the TBs and the free surface [37]

4 Plastic Deformation in Metallic Glass Matrix Composites

Metallic glasses (MGs) have attracted tremendous attention in the past few decades due to their superior mechanical properties such as high elastic limit, remarkable hardness, high fracture toughness, and good corrosion resistance [40–43]. MGs in their bulk form suffer from a strong tendency to plastic strain localization in a narrow region called shear band and exhibit macroscopically catastrophic failure under tension at room temperature. A great deal of effort has been made in recent years to improve the plasticity of MGs. Some monolithic MGs exhibiting considerable compressive plasticity were developed, possibly due to a high Poisson's ratio with the relative ease of shearing over dilatation [43], in situ nanocrystallization during deformation [44], and more free volume by faster cooling [45] or minor alloying

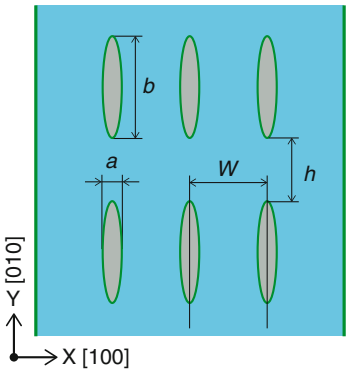

Fig. 13 Schematic of a MG-matrix composite model containing second-phase nanocrystals with dimensions of 78.5 × 84.2 × 5.6 nm^3. The orientation of the nanocrystals is indicated as [100] along the X-axis and [010] along the Y-axis. The nanocrystal pattern can be adjusted by varying the geometry parameters *a*, *b*, *w*, and *h*. Uniaxial tension is applied along the Y-axis. Free surface condition is applied along the X-axis [50]

[46]. However, MGs still show limited plastic strain under tension. In order to overcome this issue, MG/crystal composites have recently been developed by virtue of the interaction between the glass matrix and crystalline particles. Remarkable tensile ductility of these composites has been reported [47–49]. This section will be focused on the microstructural evolution and deformation mechanisms of a crystal-reinforced MG composite model with discontinuous Cu particles inserted into a $Cu_{64}Zr_{36}$ glass matrix (Fig. 13). By controlling the size, spacing, and orientation of the nanocrystals, various patterns of MG-matrix composites can be generated for simulations [50].

The stress-strain relations of the MG-matrix composites with three different shapes of $b/a = 6.5$, 5.7, and 3.7 are shown in Fig. 14a, while the normalized number of atoms in shear transformation zones (STZs) in the glass matrix is plotted against the applied strain in Fig. 14b. At the initial elastic deformation range, the tensile stresses of the composites increase linearly with the applied strain. At about 7% strain, local STZs start to nucleate in the glass matrix, as shown in Fig. 14c. The global yielding of the sample is a result of STZ localization and the formation of embryo shear bands at the free surface and glass-crystal interfaces, as shown in Fig. 14d. The thickness of these embryo shear bands is ~10 nm. It is seen that the normalized number of STZ atoms increases radically at this time (see Fig. 14b). In the stress-strain curves, this is registered as an abrupt stress drop (see Fig. 14a). Interestingly, the stress drops of the MG-matrix composites are noticeably smaller than that of the monolithic MG sample (~2 GPa). The underlying deformation mechanisms are illustrated in Fig. 14e, f. It is seen that, as the embryo shear bands evolve in the glass matrix, the nanocrystals act as barriers to shear band propagation. Some shear bands cease their propagation due to the suppression of nanocrystals, while others deviate from

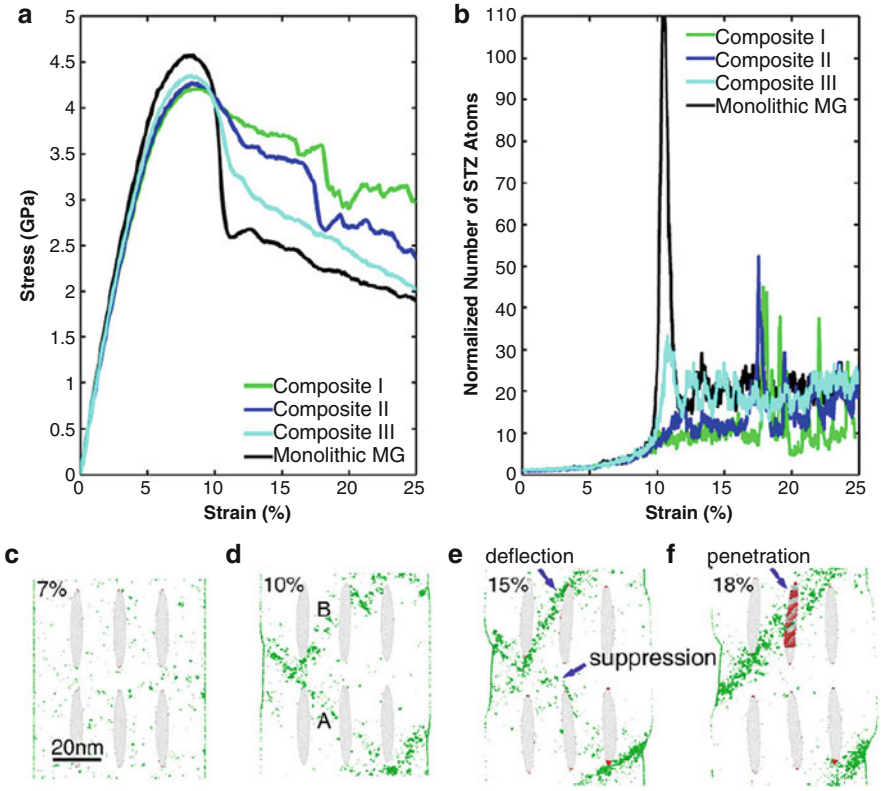

Fig. 14 (**a**) Typical stress-strain curves of MG-matrix composites with various shapes of nanocrystals. (**b**) The relations between the normalized number of STZ atoms in the glass matrix and the applied strain. (**c**–**f**) Atomistic configurations of a MG-matrix composite showing suppression and deflection of shear bands by nanocrystals [50]

their original shear path and deflect along the glass-crystal interfaces. In this way, shear localization might be effectively suppressed in the glass matrix, improving the global plasticity of the composites.

As the volume fraction of the nanocrystals increases to ~50%, the glass matrix becomes limited for the formation of embryo shear bands. Figure 15a shows that, at this relatively large volume fraction, STZs are uniformly distributed in the glass matrix at 13% strain and no localized deformation in the form of shear bands is observed, in distinct contrast to the case with a lower volume fraction of 14.5% shown in Fig. 14d. The blue arrow in Fig. 15a indicates that the operation of STZs near the glass-crystal interfaces can trigger the emission of dislocations from the interface. Further plastic deformation of this composite is thus governed by the cooperative operations of dislocations in the nanocrystals and STZs in the glass matrix, as shown in Fig. 15b.

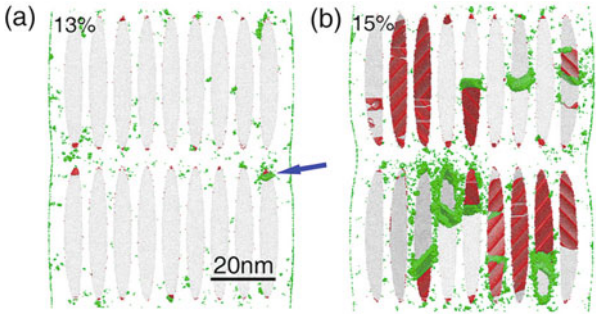

Fig. 15 (**a**, **b**) Atomic configurations of a composite with a large volume fraction of nanocrystals at two different applied strains. The arrow indicates the activation of lattice dislocations at the glass-crystal interfaces [50]

5 Non-localized Deformation in Metallic Alloys with Amorphous Structure

It has been argued that atomic-, nano-, and microscale spatial fluctuations in material density and strength may play important roles in the mechanical behavior of MGs [51–53]. Inspired by the concept of heterogeneous microstructures, pre-plastic deformation by compression or cold-rolling was performed to improve the plasticity of MGs during subsequent bending and compression tests, which is attributed to the introduction of pre-existing shear bands during pre-deformation [54, 55]. The cold-rolled MGs even exhibited an obvious plastic deformation during tension [56, 57]. The underlying mechanism of how the pre-existing shear bands affect the deformation behavior of MGs, however, is still unclear. This section is focused on understanding the deformation mechanisms of MGs with tailor-designed pre-existing shear bands. The simulation details can be found in Ref. [58]

Stress-strain curves for MGs with a composition of $Cu_{64}Zr_{36}$ and various atomic percents of pre-existing shear bands that are aligned parallel to the loading axis are shown in Fig. 16a. It is seen that the macroscopic yield stress decreases as the atomic percent of pre-existing shear bands increases from 0 at.% to 7.38 at.%. It is interesting that the flow stress after the stress overshoot first increases with increasing amount of pre-existing shear bands in the range of 0 at.% to 3.27 at.% and then reaches a plateau as the atomic percent further increases from 3.43 at.% to 7.38 at.%. The contrast is also observed in Fig. 16b, where the normalized number of atoms in STZs is plotted against the applied strain. It is clear that after sample yielding, the number of STZ atoms increases rapidly for samples with less than 3.43 at.% pre-existing shear bands, while it remains on a plateau for samples with more pre-existing shear bands.

Deformation patterns of samples with 3.27 at.% and 3.42 at.% pre-existing shear bands are shown in Fig. 17. Atoms in operating STZs are colored in green, while those in the pre-existing shear bands are painted in red. Figure 17a shows that a shear band of ~10 nm in width is formed in the sample with 3.27 at.% pre-existing shear bands at a total strain of 12%. The sample features two shear offsets on the free surfaces. The shear localization first appears in the glass matrix near the surface and

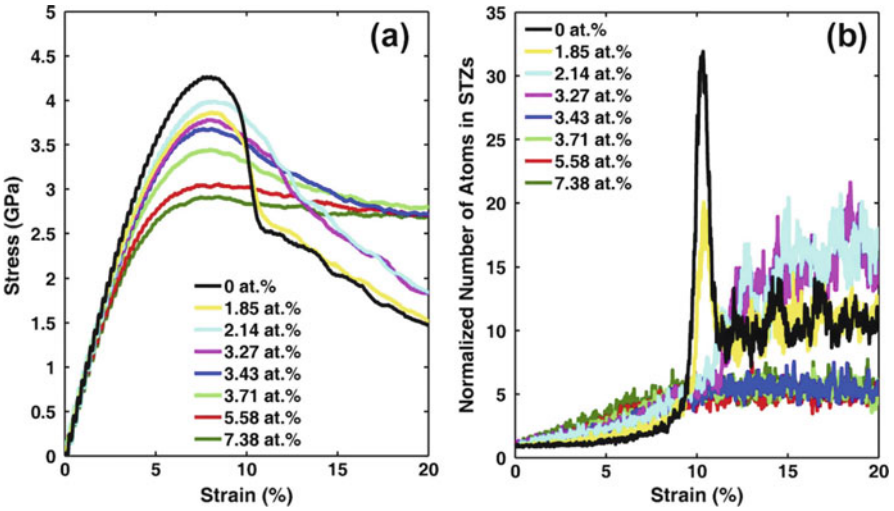

Fig. 16 Simulated stress-strain relations (**a**) and normalized number of atoms in STZs as a function of strain (**b**) for MGs with various contents of pre-existing shear bands [58]

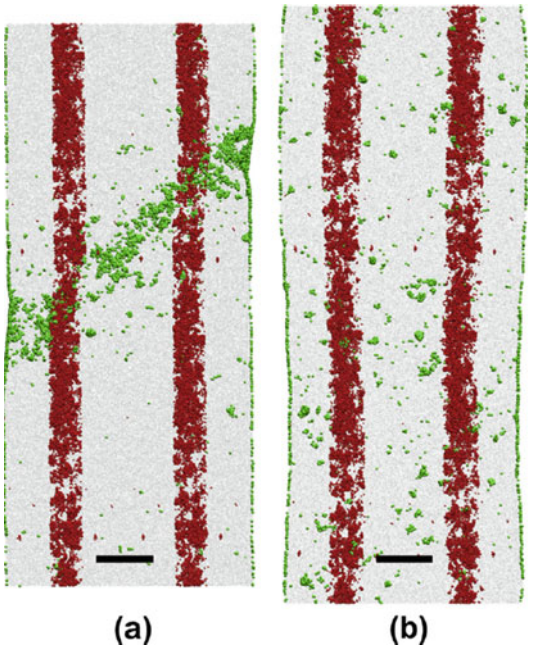

Fig. 17 Deformation patterns of two typical MGs embedded with pre-existing shear bands. (**a**) Shear band occurs in the sample with 3.27 at.% pre-existing shear bands. (**b**) Uniform STZs are observed in the sample with 3.43 at.% pre-existing shear bands [58]

then extends across the entire sample. In contrast, in the sample with a slight larger amount (3.42 at.%) of pre-existing shear bands, plasticity is dominated by non-localized deformation with slight necking at strains up to 20%, as shown in Fig. 17b. The activation of STZs is uniformly distributed, and highly localized shear banding

is suppressed during tension simulation. As a result, there exists a transition in tensile deformation of MGs at a critical atomic percent of pre-existing shear bands between 3.27 at.% and 3.43 at.%. Similar transition in plastic deformation is also observed for different orientations of pre-existing shear bands, albeit at slightly different critical atomic percents.

6 Summary

In this chapter, enhanced mechanical properties (strength, toughness, and ductility) of metallic materials by introducing structural heterogeneities, such as nanoscale twins, second-phase particles, or pre-deformed materials, have been demonstrated by MD simulations under various loading conditions (tension, indentation, and torsion). The knowledge about the underlying unique deformation mechanisms gained from these simulations not only extends the fundamental understanding of the relationship between nanoscale structures and macroscopic properties but also provides insights for future design of nanostructured metals with superior mechanical behaviors.

References

1. Koch CC, Morris DG, Lu K, Inoue A. MRS Bull. 1999;24:54.
2. Gleiter H. Acta Mater. 2000;48:1.
3. Argon AS, Yip S. Phil Mag Lett. 2006;86:713.
4. Meyers MA, Mishra A, Benson DJ. Prog Mater Sci. 2006;51:427.
5. Van Swygenhoven H, Spaczer M, Caro A, Farkas D. Phys Rev B. 1999;60:22.
6. Zhu T, Li J, Samanta A, Leach A, Gall K. Phys Rev Lett. 2008;100:025502.
7. Weinberger CR, Cai W. J Mech Phys Solids. 2010;58:1011.
8. Dai S, Xiang Y, Srolovitz DJ. Acta Mater. 2014;69:162.
9. Karaman I, Sehitoglu H, Gall K, Chumlyakov YI, Maier HJ. Acta Mater. 2000;48:1345.
10. Chen M, Ma E, Hemker K, Sheng H, Wang Y, Cheng X. Science. 2003;300:275.
11. Lu L, Shen Y, Chen X, Qian L, Lu K. Science. 2004;304:422.
12. Zhang X, Misra A, Wang H, Nastasi M, Embury JD, Mitchell TE, Hoagland RG. Appl Phys Lett. 2004;84:1096.
13. Lu K, Lu L, Suresh S. Science. 2009;324:349.
14. Hodge AM, Wang YM, Barbee TW Jr. Scripta Mater. 2008;59:163.
15. Tian Y, et al. Nature. 2013;493:385.
16. Wang YM, Sansoz F, Lagrange T, Ott RT, Marian J, Barbee TW Jr, Hamza AV. Nature Mater. 2013;12:697.
17. Huang Q, et al. Nature. 2014;510:250.
18. Wei YJ, et al. Nat Commun. 2014;5:3580.
19. Shin YA, et al. Nat Commun. 2016;7:10772.
20. Li XY, Wei YJ, Lu L, Lu K, Gao HJ. Nature. 2010;464:877.
21. Lu L, Chen X, Huang X, Lu K. Science. 2009;323:607.
22. Jang D, Li XY, Gao HJ, Greer JR. Nature. Nanotechnol. 2012;7:594.
23. Bufford D, Wang H, Zhang X. Acta Mater. 2011;59:93.
24. You ZS, Lu L, Lu K. Acta Mater. 2011;59:6927.
25. You ZS, Li XY, Gui LJ, Lu QH, Zhu T, Gao HJ, Lu L. Acta Mater. 2013;61:217.

26. Misra A, Hirth JP, Hoagland RG. Acta Mater. 2005;53:4817.
27. Li YP, Zhang GP. Acta Mater. 2010;58:3877.
28. Zhou HF, Li XY, Qu SX, Yang W, Gao HJ. Nano Lett. 2014;14:5075.
29. Qu SX, Zhou HF. Nanotechnology. 2010;21:335704.
30. Was GS, Foecke T. Thin Solid Films. 1996;286:1.
31. Nix WD. Scripta Mater. 1998;39:545.
32. Mishin Y, et al. Phys Rev B. 2001;63:224106.
33. Qin EW, Tao NR, Lu K. Scripta Mater. 2009;60:539.
34. Singh A, Tang L, Dao M, Lu L, Suresh S. Acta Mater. 2011;59:2437.
35. Dao M, Lu L, Shen YF, Suresh S. Acta Mater. 2006;54:5421.
36. Zhou HF, Qu SX, Yang W. Model Simul Mater Sci Eng. 2010;18:065002.
37. Zhou HF, Li XY, Wang Y, Liu ZS, Yang W, Gao HJ. Nano Lett. 2015;15:6082.
38. Wang J, et al. Acta Mater. 2010;58:2262.
39. Li B, Sui M, Ma E, Mao S. Phys Rev Lett. 2009;102:205504.
40. Johnson WL. MRS Bull. 1999;24:42.
41. Ashby MF, Greer AL. Scripta Mater. 2006;54:321.
42. Inoue A, Shen BL, Koshiba H, Kato H, Yavari AR. Nature Mater. 2003;11:661.
43. Schroers J, Johnson WL. Phys Rev Lett. 2004;93:255506.
44. Chen MW, Inoue A, Zhang W, Sakurai T. Phys Rev Lett. 2006;96:245502.
45. Chen LY, et al. Scripta Mater. 2008;59:75.
46. Chen LY, et al. Phys Rev Lett. 2008;100:075501.
47. Hays CC, Kim CP, Johnson WL. Phys Rev Lett. 2000;84:2901.
48. Hofmann DC, et al. Nature. 2008;451:1085.
49. Wang YM, Li J, Hamza AV, Barbee TW Jr. Proc Natl Acad Sci. 2007;104:11155.
50. Zhou HF, Qu SX, Yang W. Inter J Plast. 2013;44:147.
51. Murali P, Guo TF, Zhang YW, Narasimhan R, Li Y, Gao HJ. Phys Rev Lett. 2011;107:215501.
52. Ohkubo T, Nagahama D, Mukai T, Hono K. J Mater Res. 2007;22:1406.
53. Das J, et al. Phys Rev Lett. 2005;94:205501.
54. Yokoyama Y, Yamano K, Fukaura K, Sunada H, Inoue A. Scripta Mater. 2001;44:1529.
55. Yokoyama Y. J Non-Cryst Solids. 2003;316:104.
56. Yokoyama Y, Fukaura K, Inoue A. Intermetallics. 2002;10:1113.
57. Cao QP, et al. Acta Mater. 2010;58:1276.
58. Zhou HF, et al. Acta Mater. 2014;68:32.